ROYAL SOCIETY OF CHEMISTRY

Check for updates

Interfacial energy storage in aqueous zinc-ion batteries

Yuhang Dai, [ID] †*[a] Chengyi Zhang,†[c] Xinyu Zhang,[b] Peie Jiang,[ab] Jie Chen, [ID] [b] Wei Zong, [ID] [a] Sicheng Zheng,[b] Xuan Gao,*[b] Thomas J. Macdonald[d] and Guanjie He [ID] *[b]

Aqueous zinc-ion batteries (AZIBs) are attractive for large-scale energy storage due to their intrinsic safety, low cost, and environmental compatibility. However, the high charge-to-radius (q/r) ratio of Zn^{2+} leads to strong solvation and sluggish solid-state diffusion, which hinder efficient charge transport across solid–solid and solid–liquid interfaces. These limitations reduce both cycling stability and rate performances. In this review, we summarize interfacial transport regulation strategies, including solid–solid interfacial modulation *via* electrostatic fields, interfacial bonding, and ion–electron decoupling to enhance solid-state Zn^{2+} mobility. We further discuss solid–liquid interfacial desolvation regulation including water activity control, solvation structure tuning, and selective ion channels to mitigate desolvation barriers. We also describe emerging mechanisms involving water dissociation at interfaces, where protons and hydroxide ions act as alternative charge carriers. These unconventional pathways can complement or even outperform traditional Zn^{2+} intercalation. Collectively, these interfacial strategies not only accelerate Zn^{2+} transport but also introduce new electrochemical phenomena that boost capacity and rate performances of AZIBs. Advancing the deliberate design and mechanistic understanding of such interfacial processes will be essential to unlocking the full potential of next-generation AZIBs.

Broader context

The development of safe, long-lasting, and cost-effective energy storage technologies is essential for the widespread integration of renewable energy. Aqueous zinc-ion batteries (AZIBs) have attracted increasing interests due to their intrinsic safety, non-flammable water-based electrolytes, and the low cost and abundance of their electrode materials. These advantages make AZIBs promising for grid-scale storage, peak-shaving, and fast-charging applications. However, their practical performance remains limited by interfacial challenges, as Zn^{2+} ions interact strongly with both solid electrodes and water molecules in the solvation shell. Problems such as dendrite growth, parasitic water decomposition reactions, and sluggish ion transport have not yet been fully resolved. While advances in material and electrolyte design have yielded significant improvements, interfacial regulation is increasingly recognized as a key factor that directly governs Zn^{2+} migration and overall electrochemical performance. Recent studies suggest that rationally engineered interfaces can not only suppress degradation but also boost capacity and charging rates. Notably, emerging studies revealed that water dissociation products, such as protons and hydroxide ions, can actively participate in charge storage, enabling unconventional mechanisms beyond Zn^{2+} insertion. Continued advances in understanding and controlling interfacial processes will be essential for realizing the full potential of AZIBs in practical energy storage systems.

1. Introduction

Since 2012, aqueous zinc-ion batteries (AZIBs) have been extensively investigated as promising candidates for large-scale energy storage because they combine cost-effectiveness and environmental sustainability.[1–4] In addition, the use of water-based electrolytes eliminates fire risks and enables safer operation compared to conventional lithium-ion batteries.[5] These advantages render AZIBs attractive for grid balancing, backup storage, and fast-charging applications. They are especially suitable for scenarios where safety, long cycle life, and high power density are critical.[6]

[a] *Department of Engineering Science, University of Oxford, Oxford OX1 3PJ, UK. E-mail: yuhang.dai@eng.ox.ac.uk*

[b] *Christopher Ingold Laboratory, Department of Chemistry, University College London, London WC1H 0AJ, UK. E-mail: xuan.gao.21@ucl.ac.uk, g.he@ucl.ac.uk*

[c] *School of Chemical Sciences, The University of Auckland, Auckland 1010, New Zealand*

[d] *Department of Electronic and Electrical Engineering, University College London, London WC1E 7JE, UK*

† These authors contribute equally.

9018 | *Energy Environ. Sci.*, 2025, **18**, 9018–9030

This journal is © The Royal Society of Chemistry 2025

Despite these advantages, the practical deployment of AZIBs remains hindered by intrinsic scientific challenges. The key issue stems from the high charge density and small ionic radius of Zn^{2+} (+2, 0.74 Å),[7] compared to Li^+ (+1, 0.76 Å),[8] resulting in much stronger electrostatic interactions with host lattices and coordinated water molecules in its solvation shell. Consequently, Zn^{2+} experiences sluggish solid-state diffusion and a high desolvation (removal of coordinated solvent molecules from ions prior to insertion into the host material) penalty at electrode–electrolyte interfaces. These limitations induce uneven Zn plating, dendrite formation, parasitic side reactions such as hydrogen evolution, and structural degradation of cathode materials through dissolution or distortion, ultimately impairing cycling stability and overall efficiency.

To tackle these challenges, extensive efforts have been devoted to both electrode and electrolyte design. On the cathode side, phase engineering, pre-intercalation strategies,[9] and anion redox mechanisms[10] have been explored to stabilize host structures and promote Zn^{2+} storage. Electrolyte engineering has primarily targeted the bulk solvation environment of Zn^{2+} through highly concentrated electrolytes (water-in-salt systems[11]), eutectic formulations,[12] solvation structure modulation via donor number adjustments,[13] and diverse additives, whose functional groups can critically modulate solvation structure and interfacial chemistry to mitigate side reactions.[14–16] For zinc metal anodes, crystallographic orientation control has been employed to suppress dendrite growth and improve reversibility.[17]

In parallel, interfacial regulation has increasingly emerged as a systematic strategy to address multiple bottlenecks that fundamentally govern Zn^{2+} transport and reaction kinetics. Integrated with the European initiative Battery 2030+, which underscores the importance of interface control for future battery innovation, recent interfacial designs in AZIBs encompass solid–solid composite architectures within cathodes,[18] protective interphases at electrode–electrolyte interfaces,[19] and Zn anode modifications such as cation-adsorbed shielding layers.[20] These approaches collectively enhance Zn^{2+} mobility, facilitate desolvation, suppress parasitic reactions, and enable additional reaction pathways related to interfacial water dissociation, thereby improving energy density and cycling stability especially under high-rate cycling conditions.

Herein, recent advances in interfacial regulation of Zn^{2+} transport are systematically summarized. We specifically focus on interfacial phenomena that govern charge storage and reversibility, rather than providing a comprehensive survey of all aspects of AZIBs such as Zn anode morphology or full-cell engineering. In contrast to previous reviews that largely emphasize Zn anodes or electrolyte design, our work complements them by highlighting cathode-side interfacial regulation.[21–26] Within this scope, we integrate mechanistic insights to uncover emerging interfacial processes in which water dissociation products directly participate in charge storage. These insights reveal unconventional capacity gains and exceptionally fast kinetics. A deeper mechanistic understanding of interfacial Zn^{2+} transport is expected to inform novel design principles for next-generation high-performance aqueous zinc-ion batteries.

2. Regulation of Zn^{2+} transport at solid–solid interfaces

The design of solid–solid interfaces plays a pivotal role in addressing ion transport limitations within electrode materials. The strong electrostatic interaction between Zn^{2+} and host lattices often results in sluggish solid-state diffusion, which becomes particularly pronounced under practical high-loading conditions. By rationally engineering heterointerfaces within composite materials, it is possible to modulate local electrostatic fields, establish interfacial chemical bonding, and spatially decouple ion and electron transport pathways, thereby enabling more efficient Zn^{2+} migration across solid–solid interfaces.

2.1 Electrostatic modulation of Zn^{2+} migration

Electrostatic regulation at solid–solid heterointerfaces has been demonstrated as an effective strategy to accelerate Zn^{2+} migration by lowering the diffusion energy barrier. In particular, constructing built-in electric fields reshapes the local charge distribution, thereby enhancing Zn^{2+} adsorption and facilitating ion transport. A representative example is the $H_2V_3O_8$–MXene heterostructure, where charge redistribution across the interface induces a strong internal electric field that promotes Zn^{2+} migration (Fig. 1(a)–(c)).[27] Density functional theory (DFT) calculations revealed that the Zn^{2+} migration barrier was significantly reduced from 3.4 eV in pure $H_2V_3O_8$ to 1.3 eV at the interface, accompanied by distinct charge transfer and increased electron density near the Fermi level. This combination improves both electronic conductivity and Zn^{2+} diffusion kinetics.

Similar electrostatic modulation effects have been reported in various heterointerface systems. For instance, the V_2C–V_2O_5 heterostructure forms a highly polarized interface that strengthens the local electric field, enhancing Zn^{2+} adsorption and reducing migration barriers.[28] Likewise, the Cu-HHTP–MXene (HHTP = 2, 3,6,7,10,11-hexahydroxytriphenylene) hybrid forms extended two-dimensional channels with open coordination environments that facilitate Zn^{2+} transport under the influence of interfacial electric fields.[29] In another example, MnO–nitrogen-doped graphene aerogel (NGA) composites leverage interfacial charge redistribution from MnO–NGA interactions to promote Zn^{2+} migration.[30] Interfacial polarization has also been exploited in MoS_2–MXene heterostructures, where strong interlayer interactions contribute to reduced Zn^{2+} diffusion barrier.[31] In another case, poly(3,4-ethylenedioxythiophene) (PEDOT) modified V_2O_5 nanosheets exhibit improved Zn^{2+} storage kinetics by facilitating capacitive behaviors through an enhanced surface charge density.[32]

Collectively, these studies demonstrate that engineering built-in electric fields at heterointerfaces provides an efficient means to regulate Zn^{2+} adsorption and migration, offering improved charge transfer and fast ion transport pathways.

2.2 Interfacial chemical bonding pathways

In addition to electrostatic effects, constructing interfacial chemical bonds offers another effective route to regulate Zn^{2+} migration. Chemical bonding at the interface serves as anchor points that stabilize the inserted Zn^{2+}, lower diffusion barriers,
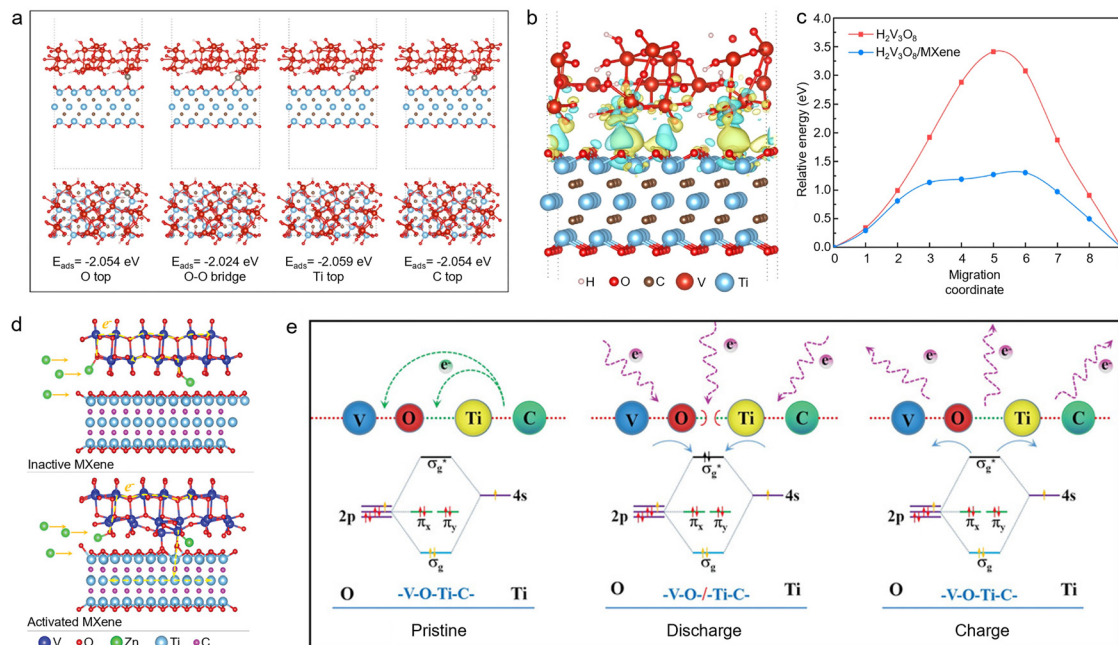
Fig. 1 Solid–solid interfacial regulation of Zn^{2+} transport through electrostatic fields and chemical bonding. (a) DFT-calculated Zn^{2+} adsorption energies on $H_2V_3O_8$–MXene interface with various configurations. (b) Charge density difference showing interfacial charge redistribution. (c) Zn^{2+} migration barriers on pristine $H_2V_3O_8$ and $H_2V_3O_8$–MXene interface. Reproduced from ref. 27. Copyright (2022), with permission from Elsevier. (d) Schematic of interfacial activation and Zn^{2+} transport pathways enabled by V–O–Ti–C bonding. (e) Dynamic evolution of V–O–Ti bonds during cycling, facilitating reversible Zn^{2+} insertion. Reproduced from ref. 33. Copyright (2023), with permission from Wiley-VCH.

and create directional pathways for ion movement. A representative example is the V_5O_{12}–Ti_3C_2 heterostructure, where dynamic V–O–Ti bonds form at the interface and actively participate during cycling (Fig. 1(d) and (e)).[33] These bonds undergo reversible breaking and reformation as Zn^{2+} inserts and extracts, buffering volume changes while maintaining structural integrity and delivering high capacity with excellent stability.

Various other heterostructures have implemented similar bonding strategies to regulate Zn^{2+} transport. Specifically, in VO_2@Co–N–C composites, atomically dispersed Co–N coordination centers form Co–O–V bonds with VO_2, which modulate local charge distribution and facilitate Zn^{2+} adsorption and directional diffusion.[34] Similarly, the V_2O_5@NC system introduces nitrogen-doped carbon interfaces that generate V–O–C bonds, guiding Zn^{2+} migration while stabilizing structural frameworks.[35] In another case, the IC@MnO_2 material introduces positively charged interstitial carbon (IC) into the MnO_2 lattice, leading to the formation of Mn–O–C bonds. These interfacial bonds facilitate simultaneous Zn^{2+} and H^+ intercalation, improving both capacity and reversibility.[36] In addition to these examples, the V_2C–V_2O_5 and Cu-HHTP–MXene heterostructures also exhibit interfacial bonding features that contribute to the Zn^{2+} transport enhancement alongside their electrostatic effects.[28,29]

These interfacial bonding configurations offer tunable energy landscapes that enable fast, directional Zn^{2+} migration with suppressed structural degradation, providing an attractive pathway for high-rate AZIBs.

2.3 Ion–electron decoupling at composite interfaces

Beyond controlling ion migration barriers, spatial decoupling of electron and Zn^{2+} transport (separating the pathways of electron and ion transport), a concept originating from lithium-ion systems, provides a distinct strategy to achieve both high capacity and rapid charge storage.[37] This "job-sharing" mechanism creates heterointerfaces where Zn^{2+} and electrons are stored and transported in separate yet adjacent domains. A typical example is the VO_x–reduced graphene oxide (rGO) composite,[38] where Zn^{2+} ions are predominantly stored in regions where sub-nanometer VO_x clusters are loaded onto rGO, as shown in the scanning transmission electron microscopy (STEM) image (Fig. 2(a)). This suggests that ion storage sites are jointly defined by both VO_x and rGO. Mechanistically, interfacial V–O–C bonds in the pristine state convert into V–O–V bonds during Zn^{2+} insertion, as confirmed by Raman spectroscopy (Fig. 2(c)), indicating Zn^{2+}-induced interfacial bond reconstruction. Electron energy loss spectroscopy (EELS) further shows an increase in the vanadium valence state during charging (Fig. 2(d)), confirming redox activity localized at VO_x sites. Meanwhile, enhanced π–π* shake-up signals observed in the rGO (Fig. 2(e)) indicate electron delocalization through the conductive carbon network, corroborating the spatial separation of electron and ion pathways.

Together, these findings reveal a decoupled transport mechanism in which Zn^{2+} ions are stored *via* redox reactions on VO_x, while electrons are conducted through rGO (Fig. 2(b)). Galvanostatic intermittent titration technique (GITT) measurements in this work further reveal that the Zn^{2+} diffusion
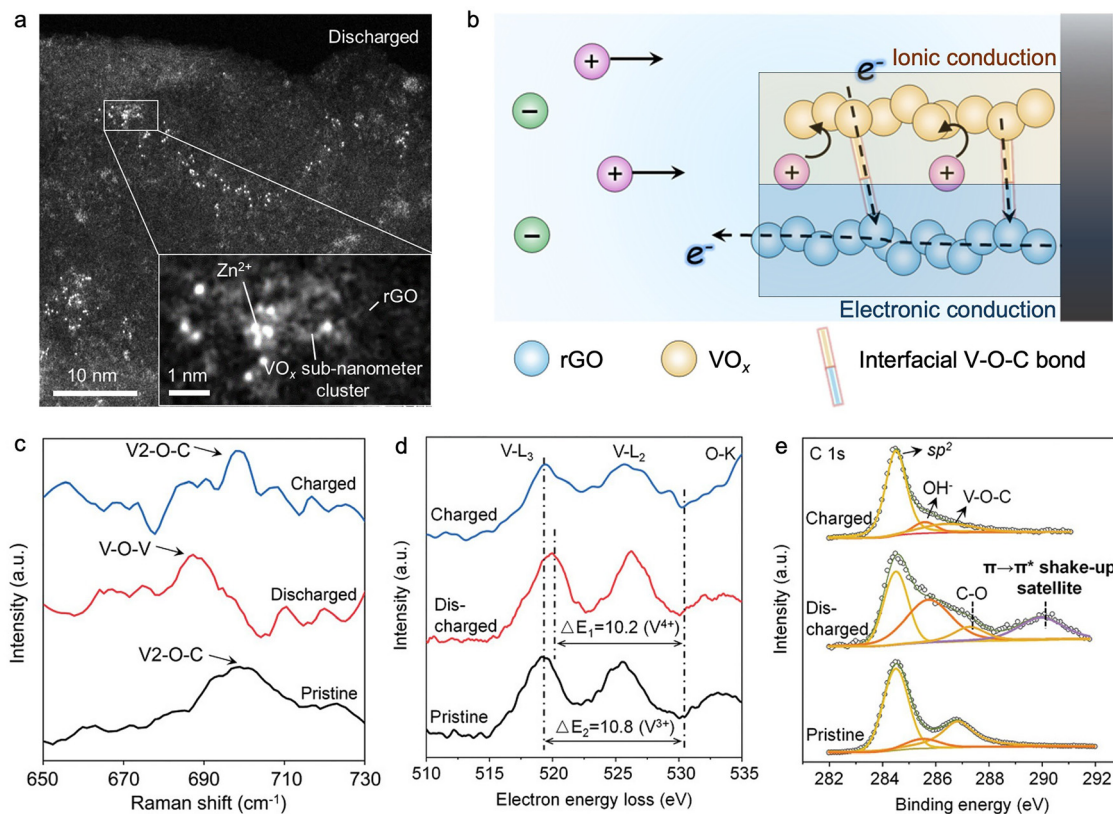
9020 | *Energy Environ. Sci.*, 2025, **18**, 9018–9030

This journal is © The Royal Society of Chemistry 2025

Fig. 2   Solid–solid interfacial regulation of Zn^{2+} transport through electron–ion decoupling. (a) STEM image of VO_x–rGO showing VO_x clusters and Zn^{2+} storage at the interface. (b) Schematic of spatially separated Zn^{2+} storage and electron conduction enabling pseudocapacitive behavior. (c) Raman spectra tracking V–O–C bond changes upon cycling. (d) EELS analysis of vanadium valence evolution. (e) C 1s XPS spectra showing V–O–C bonding and π–π^* signals. Reproduced from ref. 38. Copyright (2023), with permission from Wiley-VCH.

coefficient of VO_x–rGO is over two orders of magnitude higher than that of bulk VO_2, corroborating the markedly accelerated ion transport enabled by the decoupled electron/ion pathways. This system delivers a high specific capacity of 443 mAh g^{-1} at 100 mA g^{-1} and maintains excellent rate capability, retaining 174.4 mAh g^{-1} at 100 A g^{-1}. Moreover, the charge storage process is governed by pseudocapacitive (surface-controlled fast charge storage process) behavior, and such an interfacial Zn^{2+} storage strategy sustains high-rate performance even at practical mass loadings up to 12.72 mg cm^{-2} (3.67 mAh cm^{-2} at 1.27 mA cm^{-2}). In addition, its facile synthesis process offers promising scalability for large-scale electrode fabrication.

The job-sharing principle has been extensively explored in VO_x–graphene oxide (GO) composites by Liu *et al.*, where hydrogen-bonded N···H–O interfaces further enhance charge separation and ion storage efficiency.[39] In this system, Zn^{2+} ions are selectively adsorbed onto the VO_x domains, while electrons are delocalized within the GO sheets, collectively establishing interfacial intercalation pseudocapacitance characterized by rapid kinetics and minimal vanadium redox fluctuation. Quantitative analyses revealed that more than 90% of Zn^{2+} storage occurred at the interface, while bulk contributions remained negligible. The hydrogen-bonded interface also imparted a self-healing capability, enabling stable long-term cycling even at high mass loadings.

These interface-governed job-sharing designs offer a unique pathway to simultaneously enhance Zn^{2+} diffusion, electron conductivity, and structural stability, thereby enabling AZIBs with both high capacity and fast charge–discharge characteristics.

Despite their advantages, these solid–solid interfacial strategies also present trade-offs. Electrostatic field designs often require complex heterostructures, interfacial bonding may hinder Zn^{2+} transport if overly strong, and ion–electron decoupling relies on added conductive frameworks that can increase material complexity. Balancing structural benefits with synthetic feasibility remains essential for their practical deployment.

3. Regulation of desolvation at solid–liquid interfaces

3.1   Cathode–electrolyte interfacial desolvation

The desolvation of hydrated Zn^{2+} prior to intercalation into cathode materials strongly influences interfacial kinetics. Regulating interfacial environments has enabled multiple strategies to accelerate desolvation while maintaining interfacial stability.

3.1.1 Water masking strategy. Water masking represents an effective strategy to lower the desolvation barrier at the cathode–electrolyte interface by modulating the Zn^{2+} solvation structure. By introducing tailored interfacial layers that selectively repel or reorient water molecules, Zn^{2+} can approach the host material with fewer coordinated water molecules, facilitating faster intercalation kinetics.

One representative example is the work by Zhong *et al.*, who introduced an interfacial desolvation enhancer (IDE) molecule that self-assembles as a monolayer on hydrated vanadium oxide cathodes.[40] As shown in Fig. 3(a)–(c), molecular dynamics simulations and coordination number analyses reveal that IDE molecules preferentially adsorb on the cathode surface, displacing interfacial H_2O molecules and reducing the number of coordinated water molecules in the Zn^{2+} solvation shell—from five in the control to four in the IDE20 system.

Importantly, IDE does not participate in the Zn^{2+} solvation shell, thereby minimizing its influence on ion size and preserving transport kinetics. This selective interfacial masking weakens Zn^{2+}–H_2O interactions and lowers the desolvation energy, resulting in enhanced rate capability and cycling stability. The IDE-coated cathodes maintain structural integrity and deliver stable performances even under high current densities.

Other studies have further illustrated water masking approaches. Gou *et al.* constructed a hydrophobic PEDOT layer inspired by biological membranes on MnO_2 cathodes, which reduced water access and promoted Zn^{2+} desolvation.[41] Furthermore, Ding *et al.* utilized F-coordination to regulate local water activity and enhance desolvation on MnO_2 surfaces.[42] These results demonstrate the broad applicability of water masking strategies to improve cathode interfacial kinetics in AZIBs.
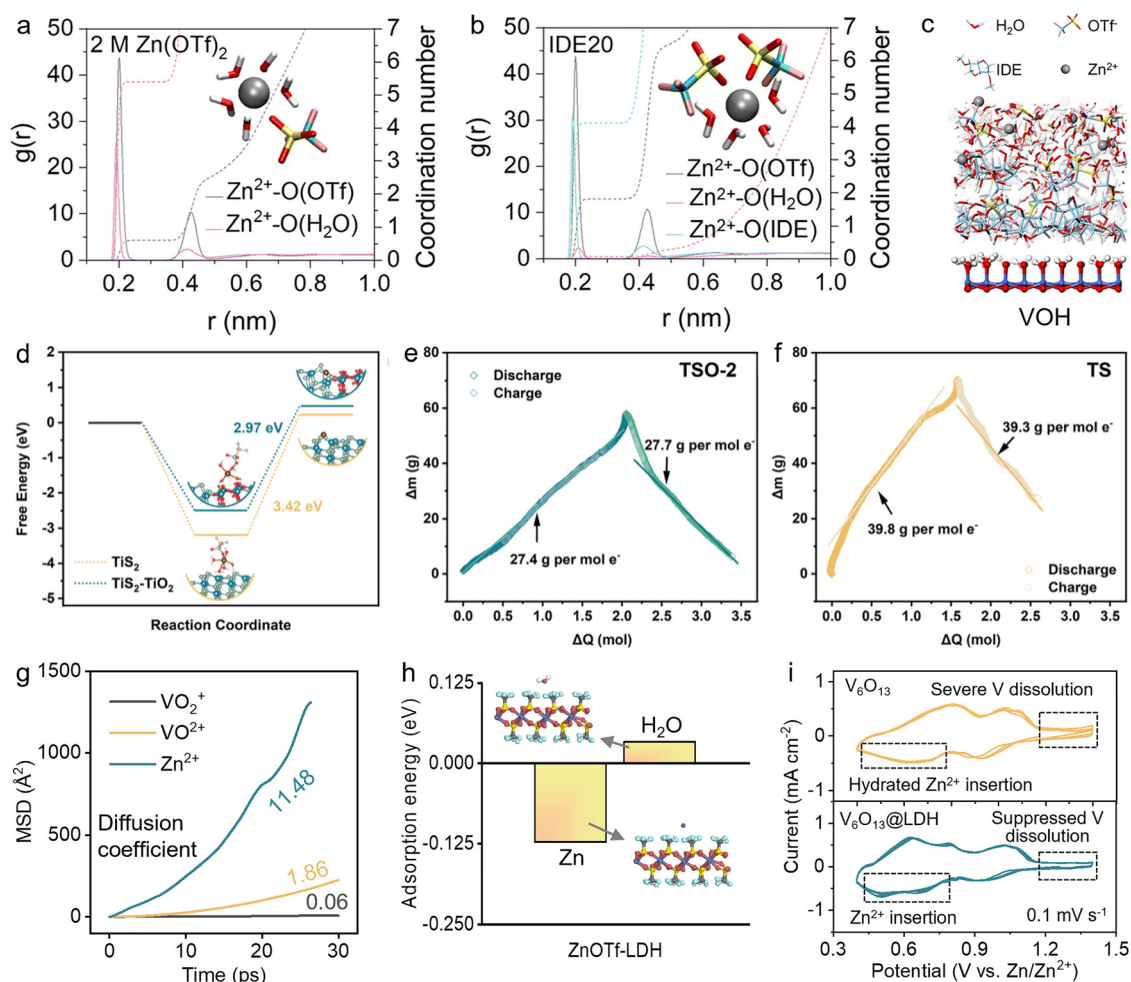

Fig. 3 Representative cathode–electrolyte interfacial desolvation regulation strategies in AZIBs. (a), (b) Radial distribution function and coordination number of Zn^{2+} with OTf^- and H_2O in 2 M $Zn(OTf)_2$ electrolyte (a) and 2 M $Zn(OTf)_2$ with 20 mM isosorbide dimethyl ether (IDE) (b). (c) Snapshot of IDE monolayer on hydrated VOH surface showing distributions of H_2O, OTf^-, and Zn^{2+}. Reproduced from ref. 40 Copyright (2024), with permission from Royal Society of Chemistry. (d) Energy barriers for the desolvation process of $[Zn(H_2O)_5]^{2+}(CF_3SO_3)^-$ on TiS_2 and TiS_2–TiO_2 surfaces. (e), (f) Mass change per mole of electron for TiS_2–TiO_2 electrode (TSO-2) (e) and pure TiS_2 electrode (TS) (f) electrodes during cyclic voltammetry (CV) scans. Reproduced from ref. 43 Copyright (2025), with permission from Wiley-VCH. (g) Mean square displacement of different ions in $Zn_x(OTf)_y(OH)_{2x-y}\cdot nH_2O$ (ZnOTf-LDH) from *ab initio* molecular dynamics (AIMD) simulations. (h) Adsorption energy of Zn^{2+} and H_2O within the channel of ZnOTf-LDH. (i) CV curves of V_6O_{13} and V_6O_{13} coated with ZnOTf-LDH at 0.1 mV s^{-1}. Reproduced from ref. 44 under the Creative Commons CC BY license.

9022 | *Energy Environ. Sci.*, 2025, **18**, 9018–9030

This journal is © The Royal Society of Chemistry 2025

3.1.2 Built-in electric field assisted desolvation. Beyond water masking, engineering internal electric fields at the cathode interface offers another pathway to accelerate Zn^{2+} desolvation. Localized electric fields can polarize incoming solvated Zn^{2+} ions, promoting partial removal of coordinated water molecules prior to Zn^{2+} intercalation.

Chen et al.[43] constructed a TiS_2–TiO_2 heterostructure that induces a built-in electric field (BIEF) via interfacial electronic redistribution between the two components. As shown in Fig. 3(d), DFT calculations reveal that the desolvation energy barrier for $[Zn(H_2O)_5]^{2+}$ complexes is significantly reduced at the TiS_2–TiO_2 interface (2.97 eV) compared to pure TiS_2 (3.42 eV), highlighting the desolvation-facilitating role of the heterojunction.

To experimentally validate this effect, the authors compared a TiS_2–TiO_2 electrode (TSO-2, prepared via 2 min O_2 plasma treatment) and a pure TiS_2 electrode (TS) using electrochemical quartz crystal microbalance (EQCM). As shown in Fig. 3(e) and (f), the TSO-2 electrode exhibits a mass change per electron ($\sim$27.4 g mol^{-1}) close to the theoretical value for bare Zn^{2+} insertion, indicating effective desolvation at the interface. In contrast, the TS electrode shows a higher mass change ($\sim$39.6 g mol^{-1}), consistent with hydrated Zn^{2+} ($[Zn(H_2O)]^{2+}$) co-intercalation. These findings confirm that the built-in electric field at the TiS_2–TiO_2 interface promotes Zn^{2+} desolvation and alters the nature of the intercalating species. Altogether, this heterostructure design mitigates strain from hydrated ion insertion, promotes fast Zn^{2+} transport, and enables high-rate cycling (e.g., 160.9 mAh g^{-1} at 5 A g^{-1}).

Complementary work by Sun et al. employed Ca^{2+} pre-intercalation in V_2O_5 to widen the interlayer spacing, which facilitates partial desolvation of Zn^{2+} upon insertion and enhances both capacity and cycling stability.[45] These lattice-level adjustments further highlight the role of interfacial field effects in regulating desolvation kinetics.

3.1.3 Artificial cathode–electrolyte interphase confinement. Beyond promoting desolvation, artificial cathode–electrolyte interphase (CEI) can also suppress active material dissolution and unwanted side reactions at the cathode surface. By confining Zn^{2+} desolvation within a well-structured interface, such designs improve long-term cycling stability.

Dai et al. designed a $Zn_x(OTf)_y(OH)_{2x-y} \cdot nH_2O$ (ZnOTf-LDH) interphase that functions as a selective ion-conducting layer on vanadium oxide cathodes.[44] As shown in Fig. 3(g), molecular dynamics simulations reveal that Zn^{2+} exhibits much higher diffusivity than VO_2^+ or VO^{2+} across the ZnOTf-LDH layer, as confirmed by their distinct mean square displacements and diffusion coefficients. This selectivity stems from stronger electrostatic interactions between ZnOTf-LDH and vanadium species, which limit their mobility. Meanwhile, Zn^{2+} is efficiently transported and partially desolvated at the interface. Fig. 3(h) shows that Zn^{2+} exhibits stronger adsorption to the ZnOTf-LDH surface compared to H_2O, reflecting the interphase's combined zincophilic and hydrophobic character. This facilitates Zn^{2+} capture while excluding water molecules and promoting the desolvation of hydrated Zn^{2+}, as evidenced by

electrochemical impedance spectroscopy (EIS) measurements at different temperatures and supporting simulations, which revealed reduced charge-transfer resistance and lower activation energy for interfacial Zn^{2+} transport. Cyclic voltammetry (CV) measurements further confirm that the ZnOTf-LDH layer stabilizes interfacial ion flux, suppresses vanadium dissolution, and maintains redox activity during cycling (Fig. 3(i)). As a result, the cathode retains capacity over extended operation. This interphase exemplifies how structural confinement and selective ion affinity can enhance both Zn^{2+} kinetics and interfacial stability.

Zheng et al.[46] applied polydopamine (PDA) coatings to $NH_4V_4O_{10}$ to create zincophilic layers that attract Zn^{2+}, lower desolvation barriers, and inhibit parasitic reactions. In a related system, Jiang et al.[47] reported PEDOT-modified $V_5O_{12} \cdot 6H_2O$ cathodes that integrate hydrophobic and zincophilic properties, enabling balanced Zn^{2+} interfacial behavior and robust cycling under various conditions.

These studies illustrate that regulating Zn^{2+} desolvation at the cathode–electrolyte interface, whether through water masking, electric field effects, or artificial interphases, offers a coherent strategy to enhance Zn^{2+} transport kinetics, suppress material degradation, and extend the operational lifetime of AZIBs.

3.2 Anode–electrolyte interfacial desolvation

Efficient Zn^{2+} desolvation at the anode interface is essential for stabilizing Zn plating and suppressing side reactions like hydrogen evolution. Although numerous strategies have been proposed for modifying Zn metal anodes, we briefly summarize three representative interfacial approaches, including catalytic regulation, electronic tuning, and solvation structure modulation. The main emphasis of this review, however, lies slightly more on cathode-side interfacial processes.

3.2.1 Atomic catalytic desolvation. Atomic-level catalysts can effectively weaken Zn^{2+}–H_2O coordination and reduce desolvation barriers. Zhang et al. anchored single Fe atoms onto $Ti_3C_2T_x$ MXene, forming SAFe@MXene interfaces that redistributed local electron density and disrupted hydration shells.[48] DFT calculations revealed that interfacial charge redistribution induced by atomic Fe significantly lowered the energy barrier for stepwise Zn^{2+} dehydration (Fig. 4(a)). Specifically, the desolvation energy for $[Zn(H_2O)_6]^{2+}$ progressively decreased with each water molecule removed, and this energy barrier was consistently lower at the SAFe@MXene interface compared to pristine Zn. In addition, adsorption energy calculations (Fig. 4(b)) revealed that Zn atoms exhibit stronger binding to the SAFe@MXene surface (−1.26 eV) compared to MXene (−0.88 eV) and pristine Zn (−0.11 eV), confirming the enhanced Zn^{2+} affinity at the engineered interface. These theoretical insights support the observed electrochemical improvements, including enhanced Zn plating reversibility and effective suppression of dendrite growth under harsh cycling conditions. Related catalytic designs have also been proposed using crown ether additives,[49] pore-sieving structures,[50] and CeO_{2-x} catalytically active suspension electrolytes.[51]

This journal is © The Royal Society of Chemistry 2025

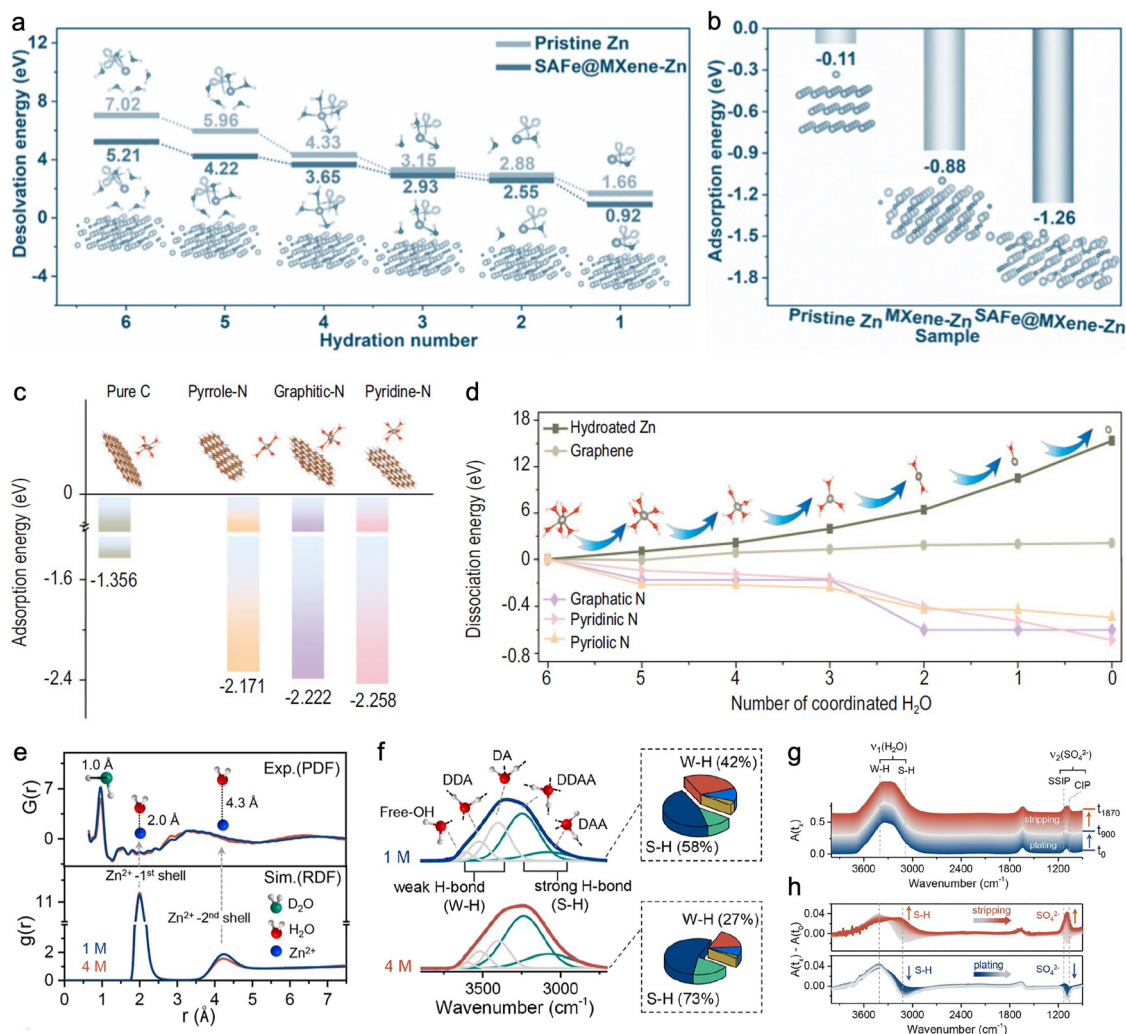Energy Environ. Sci., 2025, 18, 9018–9030 | 9023

Fig. 4 Representative anode−electrolyte interfacial desolvation regulation strategies in AZIBs. (a) DFT-calculated desolvation energy profile for stepwise Zn^{2+} dehydration on pristine Zn and SAFe@MXene-Zn surfaces (SA denotes single-atom). (b) Zn^{2+} adsorption energies on pristine Zn, MXene-Zn, and SAFe@MXene-Zn surfaces, indicating enhanced Zn^{2+} affinity at the catalytic interface. Reproduced from ref. 48 Copyright (2025), with permission from American Chemical Society. (c) DFT-calculated adsorption energies of $Zn(H_2O)_6^{2+}$ cluster on pure carbon and various nitrogen-doped carbon surfaces. (d) Dissociation energy of $Zn(H_2O)_6^{2+}$ cluster in various chemical environments. Reproduced from ref. 52 under the Creative Commons CC BY license. (e) Experimental pair distribution function (PDF) $G(r)$ (top) and simulated radial distribution function (RDF) $g(r)$ (bottom) of 1 and 4 M $ZnSO_4$ electrolytes. (f) Deconvolution of the stretching vibration of H_2O. The pie chart shows the proportions of the local weak hydrogen-bond/W-H (high wavenumber) and strong hydrogen-bond/S-H (low wavenumber). DDAA refers to a double donor−double acceptor configuration, DDA to a double donor−single acceptor, DAA to a single donor−double acceptor, and DA to a single donor−single acceptor. (g) In situ FTIR spectra were collected during the Zn-electroplating/stripping with the variation of spectra color from blue (Zn-plating, bottom) to orange (Zn-stripping, top). (h) Evolution of the relative absorbance $A(t_x) − A(t_0)$ of 1 M $ZnSO_4$ during Zn-plating (bottom) and Zn stripping (top). Reproduced from ref. 55 Copyright (2024), with permission from American Chemical Society.

3.2.2 Electronic structure-mediated desolvation. Modulating interfacial electronic structures offers a powerful approach to accelerate Zn^{2+} desolvation by altering local local charge distributions and tuning the Fermi level. Guo et al.[52] designed nitrogen-doped carbon (NC) coatings on Nafion substrates to reshape the interfacial potential landscape between Zn metal and the electrolyte. The NC layer introduced abundant non-coordinating nitrogen sites that redistributed interfacial charges and shifted the Fermi level upward, thereby destabilizing the Zn^{2+} hydration shell. As shown in Fig. 4(c), DFT

calculations indicated stronger $Zn(H_2O)_6^{2+}$ adsorption on NC, especially at pyridinic and graphitic nitrogen sites. Furthermore, the dissociation energy of $Zn(H_2O)_6^{2+}$ was markedly reduced in these nitrogen-rich environments (Fig. 4(d)), demonstrating that electronic redistribution at the interface plays a critical role in facilitating Zn^{2+} dehydration. Collectively, these effects boosted Zn^{2+} desolvation kinetics, achieving highly reversible Zn plating and mitigating dendrite formation.

Additional strategies for electronic-structure modulation include the use of molecular cage additives that offer multi-

9024 | Energy Environ. Sci., 2025, **18**, 9018–9030

This journal is © The Royal Society of Chemistry 2025

site Zn^{2+} coordination,[53] and sulfonic acid-functionalized frameworks that locally tune charge density at the interface.[54]

3.2.3 Dynamic solvation reconstruction. Revealing the dynamic nature of Zn^{2+} solvation structures under electrochemical cycling has inspired new strategies to regulate interfacial behavior. Yu et al.[55] uncovered that increasing $ZnSO_4$ concentration from 1 M to 4 M compresses the solvation shell and strengthens Zn–O interactions, as shown by molecular dynamics (MD) simulations and pair distribution function analysis (Fig. 4(e)). Time-resolved Fourier transform infrared (FTIR) spectra further revealed a progressive increase in the fraction of strong hydrogen bonds (O–H stretch at lower wavenumbers) and gradual, reversible vibrational shifts during plating/stripping (Fig. 4(f) and (g)), indicating Zn^{2+} dehydration during plating and re-solvation upon stripping. These results demonstrate that Zn^{2+} solvation is not static but dynamically reconstructs in response to the electrochemical environment (Fig. 4(h)). Aligning with this mechanistic insight, several interfacial engineering strategies have been developed to leverage dynamic solvation behavior. For example, Lu et al.[56] introduced self-assembled bio-interfacial bilayers to modulate local hydrogen-bonding networks, while Dong et al.[51] designed catalytically adaptive suspension electrolytes to promote in situ Zn^{2+} dehydration. These strategies leverage dynamic solvation reconstruction as a regulatory handle, enabling

adaptive control of Zn^{2+} flux, improve reversibility, and effective dendrite suppression.

4. Interfacial storage of species from water dissociation

4.1 H^+ storage regulation

The high hydration enthalpy of Zn^{2+}, reaching 2046 kJ mol^{-1}, not only results in significant desolvation barriers but also facilitates partial water dissociation at the electrode–electrolyte interface.[57] This interfacial hydrolysis process continuously generates additional H^+ and OH^- species, which potentially participate in charge storage reactions across multiple systems, often contributing substantial capacity beyond traditional Zn^{2+} intercalation.

4.1.1 Zn^{2+}/H^+ co-storage. In many Zn^{2+} intercalation hosts, hydrated Zn^{2+} ions and protons can simultaneously participate in the storage process, giving rise to Zn^{2+}/H^+ co-intercalation behavior. A representative example[58] is found in S-doped MoO_2. As illustrated in Fig. 5(a), the CV curve exhibits two distinct cathodic peaks, which correspond to the successive insertion of H^+ and Zn^{2+} into the electrode. Simultaneously, the in situ EQCM reveals a two-step mass change during discharge, as shown in Fig. 5(b). The first mass increase from point B to C corresponds to H^+ insertion, with a mass-to-charge ratio (m/z)
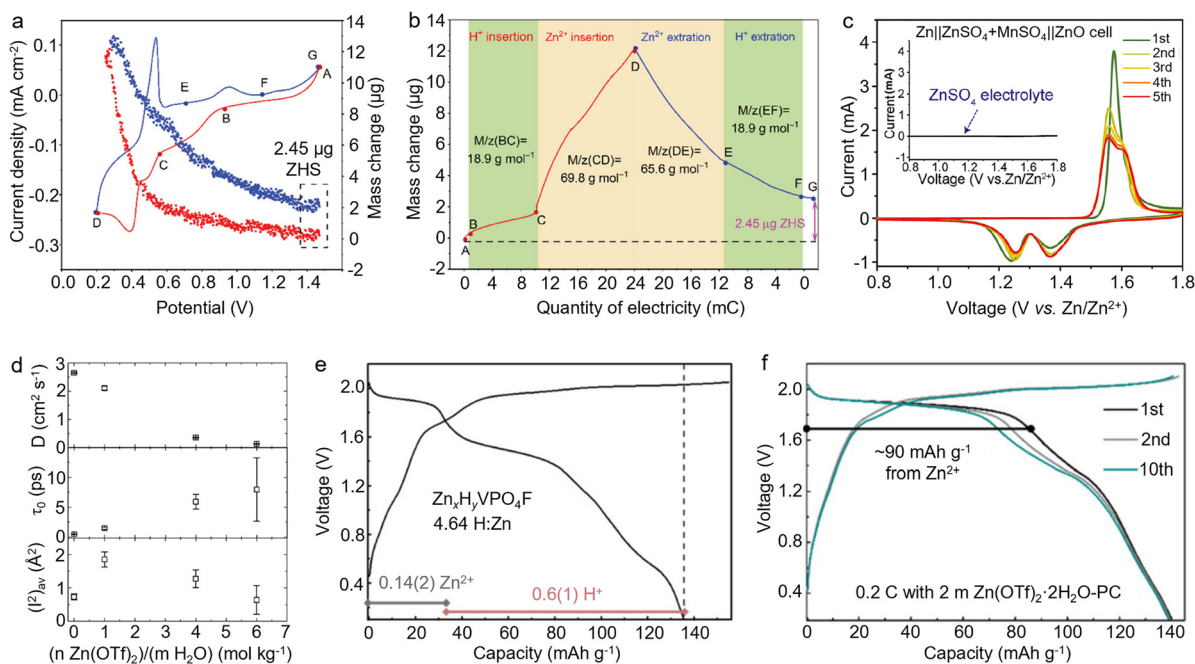

Fig. 5 Representative mechanisms of proton storage regulation in AZIBs. (a) CV curves of the aqueous Zn||S-MoO$_2$ at 1.5 mV s^{-1} and the simultaneous response of the mass change of S-MoO$_2$ electrode as recorded by EQCM. ZHS denotes basic zinc sulfate. (b) Mass weight versus charge curve during the discharging and charging process. Reproduced from ref. 58 Copyright (2023), with permission from Wiley-VCH. (c) CV curves of the Zn||2M ZnSO$_4$ + 0.5 M MnSO$_4$||ZnO cell at 0.2 mV s^{-1}, from 0.8 to 1.8 V vs. Zn/Zn^{2+}. Reproduced from ref. 63 Copyright (2022), with permission from Wiley-VCH. (d) Quasi-elastic neutron scattering (QENS) analysis of various hybrid aqueous-non aqueous (HANE) systems. (e) Typical voltage profile of VPO$_4$F between 0.2 and 2.1 V in the 4 m Zn(OTf)$_2$·H$_2$O electrolyte. Inset: H/Zn atom ratio in the discharged VPO$_4$F electrode. (f) Typical voltage profile of Zn$_x$H$_y$VPO$_4$ between 0.2 and 2.1 V in 2 m Zn(OTf)$_2$·2H$_2$O–propylene carbonate (PC) electrolyte. Reproduced from ref. 69 Copyright (2021), with permission from Wiley-VCH.

This journal is © The Royal Society of Chemistry 2025

Energy Environ. Sci., 2025, **18**, 9018–9030 | 9025

of 18.9 g mol^{-1}, matching the molar mass of H_3O^+. The subsequent sharper mass increase from point C to D yields an m/z of 69.8 g mol^{-1}, indicative of Zn^{2+} insertion coupled with formation of hydrated byproducts. During charging, the mass decrease proceeds in reverse order, with Zn^{2+} and H^+ sequentially extracted (m/z = 65.6 and 18.9 g mol^{-1}, respectively), confirming their co-contribution to the overall capacity.

Similar Zn^{2+}/H^+ co-insertion behavior has been widely observed in hydrated vanadium oxides such as $V_2O_5 \cdot nH_2O$ and VO_2. In these systems, the presence of pre-intercalated water layers provides expanded interlayer spacing and abundant hydrogen bonding sites, which effectively stabilize the co-inserted Zn^{2+} and H^+ ions. For example, in $V_2O_5 \cdot nH_2O$, quantitative analyses suggest that H^+ contributes nearly 44% of the total capacity due to its faster insertion kinetics and smaller ionic size.[59] In VO_2, Li $et\ al.$ demonstrated proton insertion with Zn^{2+} being mostly involved in surface byproduct formation.[60]

A unique H^+ "lubrication" effect has also been proposed in MoS_2-based hosts by Li $et\ al.$, where pre-inserted protons significantly lower the migration barrier for subsequent Zn^{2+} intercalation. Theoretical calculations reveal that the Zn^{2+} insertion energy barrier can be reduced from 0.97 eV to 0.41 eV upon prior H^+ insertion, thus enhancing Zn^{2+} diffusion kinetics and reversibility.[61]

4.1.2 H^+-dominated intercalation. In certain systems, H^+ serves as the exclusive or dominant charge carrier for intercalation, a behavior particularly prevalent in MnO_2-based cathodes. Using α-MnO_2 as a model system, Yuan $et\ al.$ systematically revealed that Zn^{2+} insertion is energetically unfavorable, while H^+ insertion into the 1×1 and 2×2 tunnels dominates the storage mechanism.[62] The insertion of H^+ induces slight lattice expansion and Mn–OH bond formation while preserving structural reversibility. Chen $et\ al.$[63] further revealed that the H^+-dominated intercalation mechanism does not require MnO_2 as the initial cathode material. Instead, as long as the electrode surface permits H^+ uptake ($e.g.$, Zn‖2 M ZnSO$_4$ + 0.5 M MnSO$_4$‖ZnO cell as shown in Fig. 5(c)), proton insertion triggers local OH^- enrichment and subsequent formation of $Zn_4SO_4 \cdot (OH)_6 \cdot xH_2O$ (ZHS). This ZHS layer then reacts with Mn^{2+} in the electrolyte to generate electrochemically active $Zn_xMnO(OH)_2$, which supports reversible H^+ intercalation analogous to that in conventional MnO_2-based systems. Earlier, Liu $et\ al.$[64] had also demonstrated that MnO_2 undergoes a proton-coupled conversion reaction to form MnOOH intermediates, with minimal Zn^{2+} participation.

Beyond MnO_2, proton-dominant behavior extends to other hosts. For instance, recent studies on $Na_{0.12}Zn_{0.25}V_2O_5 \cdot 2.5H_2O$ layered structures highlight highly dynamic proton conduction pathways in V_2O_5-based hosts, wherein H^+ migration proceeds via Zundel pair-dancing mechanisms, enabling ultrafast pseudocapacitive response even at extremely high current densities, effectively excluding Zn^{2+} intercalation at ultrahigh rates.[65] In parallel, in TiS_2, facet engineering enabled H^+-dominated storage with suppressed hydrogen evolution under (011) orientation.[66] Furthermore, pH and electrolyte volume have been shown to directly influence H^+ participation. Using V_2O_5

electrodes, Lee $et\ al.$[67] demonstrated that smaller electrolyte volumes or higher pH significantly suppress H^+ insertion, whereas lower pH and larger electrolyte reservoirs facilitate greater H^+ contribution.

Moreover, co-doping strategies have emerged as a powerful approach to further enhance H^+ insertion behavior. Chen $et\ al.$[68] showed that Co^{2+} pre-insertion into MnO_2 tunnels stabilizes the lattice, allowing more favorable H^+ intercalation while excluding Zn^{2+} insertion. DFT calculations revealed significantly lower migration barriers for H^+ compared to Zn^{2+} within the Co-stabilized tunnel structures, underscoring the proton-dominant storage mechanism.

4.1.3 H^+ intercalation suppression. While H^+ insertion can enhance capacity, its excessive participation may also induce structural instability and parasitic reactions such as Mn dissolution and basic zinc salt precipitation. To address this, strategies have been developed to suppress H^+ intercalation while preserving Zn^{2+} storage reversibility. Zhang $et\ al.$[69] demonstrated that VPO_4F frameworks, owing to their strong electronegativity and limited hydrogen-bonding sites, effectively exclude H^+ and favor Zn^{2+}-dominated storage. This selective behavior is supported by quasi-elastic neutron scattering (QENS) in Fig. 5(d), where reduced water mobility under concentrated $Zn(OTf)_2$ electrolytes reflects suppressed proton dynamics. Fig. 5(e) shows that $Zn_xH_yVPO_4F$ delivers a capacity corresponding to ~ 0.14 Zn^{2+} and ~ 0.6 H^+ per formula unit, indicating a dominant Zn^{2+} contribution despite residual proton uptake. Notably, Fig. 5(f) reveals stable voltage profiles over multiple cycles in a hybrid $Zn(OTf)_2 \cdot 2H_2O$–propylene carbonate (PC) electrolyte, with capacities (~ 90 mAh g^{-1}) primarily derived from Zn^{2+} insertion. These results collectively highlight the potential of tailored frameworks like VPO_4F in enabling Zn^{2+}-dominant intercalation with suppressed proton-induced side reactions, paving the way for more stable and efficient aqueous Zn-ion batteries.

It is worth noting that despite widespread discussion of "H^+ insertion," the actual origin of these protons is rarely examined in detail. At the coin cell level, quantitative analysis reveals that substantial proton involvement cannot plausibly arise from pre-existing free H^+ ions in the bulk electrolyte alone. For example, in a Zn‖VO_2 cell using a typical lab-level cathode mass of 1–5 mg and 80–200 μL of 2 M ZnSO$_4$ or 3 M Zn(OTf)$_2$ electrolyte (pH $\approx$ 4),[60,70–74] the total amount of H^+ in the bulk electrolyte is only 8–20 nmol. In contrast, experimental capacities of 250–400 mAh g^{-1} require 4–37 μmol of proton charge storage, which exceeds the available H^+ supply by more than two to three orders of magnitude. This discrepancy clearly indicates that continuous interfacial water dissociation must occur to generate additional protons during cycling. As elaborated in the following section, similar interfacial dissociation processes also underpin hydroxide-based charge storage mechanisms.

4.2 OH^- storage through water dissociation

Compared with the extensively studied Zn^{2+} and H^+ storage paradigms, OH^--based charge storage remains relatively
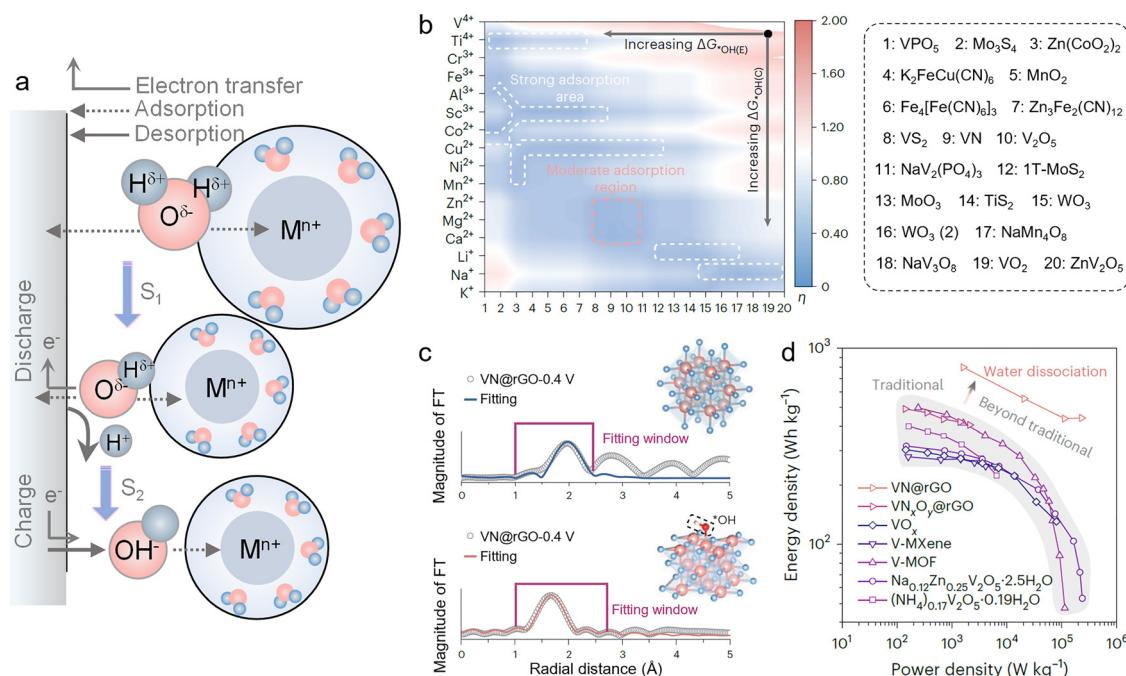
Fig. 6 Zn^{2+}-mediated interfacial OH^- storage in VN cathodes. (a) Schematic showing Zn^{2+} polarization-induced water dissociation and reversible OH^- adsorption at the electrode surface. (b) Contour plot of water dissociation activity as a function of $*OH$ adsorption energy, comparing different metal ions and cathode materials. (c) Operando extended X-ray absorption fine structure (EXAFS) fitting results indicating surface-confined $*OH$ adsorption on VN@rGO during discharge, with no lattice expansion. (d) Comparison of rate performance between water dissociation rendered OH^- storage and conventional Zn^{2+} intercalation. Reproduced from ref. 77 Copyright (2024), with permission from Springer Nature.

underexplored and mechanistically distinct, especially in mildly acidic aqueous zinc-ion battery systems. While Zn^{2+} and H^+ typically undergo intercalation, OH^- participates in surface-mediated redox reactions that proceed via confined interfacial charge transfer rather than bulk ion diffusion. This gives rise to pseudocapacitive behavior that is fundamentally different from conventional intercalation mechanisms. Recent studies have further demonstrated that OH^-, generated through interfacial water dissociation, can serve as efficient and reversible charge carriers under such conditions.

Initial evidence for OH^- involvement emerged from systems where Zn^{2+} hydrolysis leads to the formation of solid hydroxide phases such as basic zinc sulfate (ZHS), which is particularly intriguing under mildly acidic electrolytes because the generation of seemingly alkaline compounds is not straightforward. These observations indicated that Zn^{2+} could polarize adjacent water molecules, triggering water dissociation and local accumulation of OH^-. This process not only produces H^+ that may participate in intercalation mentioned above but simultaneously generates OH^- species that contribute to charge storage by being captured or fixed as solid byproducts.[75,76]

Moving beyond these indirect pathways, Dai et al.[77] recently established a catalytic model in which Zn^{2+} ions polarize adjacent water molecules, thereby facilitating continuous water dissociation at the electrode–electrolyte interface, as shown in Fig. 6(a). In this model, the OH^- species generated reversibly adsorbed at the electrode surface, with their storage kinetics primarily governed by the binding strength of $*OH$ to the

electrode surface. Through systematic screening of various combinations of cations and cathode materials, vanadium nitride (VN) was identified as the optimal candidate, featuring the most balanced Zn^{2+}–H_2O and VN–H_2O interactions, showing a moderate $*OH$ binding energy that ensures fast kinetics while minimizing side reactions, as illustrated in Fig. 6(b).

This mechanism was experimentally validated through operando (real-time and in situ) extended X-ray absorption fine structure (EXAFS) measurements, which confirmed that OH^- adsorption occurs without any detectable lattice distortion in the VN@rGO electrode. This observation supports the conclusion that charge storage takes place predominantly at the surface rather than within the bulk lattice, as depicted in Fig. 6(c). In addition, electrochemical testing revealed that VN@rGO achieves a high specific capacity of 577.1 mAh g^{-1} even at an ultrahigh current density of 300 A g^{-1}, significantly outperforming Zn^{2+}-dominated systems under comparable conditions, as shown in Fig. 6(d).

These results suggest a fundamental shift in the design principles for AZIBs. Instead of relying solely on traditional ion migration through the solid phase, this approach emphasizes interfacial catalysis as the primary mechanism governing charge storage. Careful tuning of interfacial chemistry to optimize $*OH$ adsorption enables water dissociation products, previously considered undesirable, to serve as highly effective and kinetically favorable charge carriers. It is also important to note that OH^- storage mechanisms are typically sensitive to
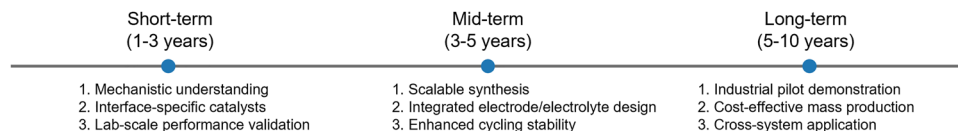
Fig. 7   Roadmap for promising interfacial design trends in AZIBs (next 5–10 years).

local pH fluctuations, which may trigger side reactions such as precipitation or phase instability over extended cycling.

5. Summary and outlook

Interfacial regulation has emerged as a powerful strategy to address the fundamental transport and stability challenges in AZIBs. This review systematically summarizes recent progresses in both solid–solid and solid–liquid interfaces, highlighting diverse yet complementary approaches for facilitating Zn^{2+} migration, desolvation, and interfacial charge transfer. At solid–solid interfaces, strategies leveraging internal electrostatic fields, interfacial chemical bonding, and electron–ion decoupling significantly reduce Zn^{2+} diffusion barriers while enhancing structural stability and reaction reversibility. For solid–liquid interfaces, engineered desolvation layers, catalytic desolvation sites, and dynamic solvation reconstruction have been successfully demonstrated to promote rapid Zn^{2+} desolvation and suppress parasitic side reactions.

Beyond classical Zn^{2+} intercalation mechanisms, recent studies have identified that products derived from interfacial water dissociation, specifically H^+ and OH^-, offer alternative and highly efficient charge storage pathways. The interfacial water dissociation mediated by Zn^{2+} polarization provides a continuous supply of H^+ and OH^-, enabling mechanisms such as H^+-dominated intercalation and surface-confined OH^- pseudocapacitance. These emerging pathways enhance battery capacity and rate capability, while redefining the role of interfacial reactions in overall performance.

Looking forward, further progress will rely on deepening mechanistic understanding of interfacial chemical dynamics under realistic operating conditions such as high mass loadings and a balanced negative-to-positive (N/P) capacity ratio. In practice, achieving a rational N/P ratio critically depends on preparing high-mass-loading cathodes, yet maintaining electrochemical performance under such conditions remains a major challenge in AZIBs.[78] Rational interfacial design is therefore expected to play a pivotal role in mitigating transport limitations and enabling stable operation at high areal capacities. To fully unravel these interfacial functions under practically relevant conditions, advanced operando characterization, multiscale simulations, and interface-specific probes are essential to resolve the intricate interplay among Zn^{2+} transport, water dissociation dynamics, and interfacial phase evolution. Moreover, deliberate design of catalytic interfaces that precisely regulate water dissociation and capture its dissociation products offers promising opportunities to break conventional

trade-offs between capacity, rate capability, and long-term stability.

While many of the interfacial strategies discussed in this review show strong potential, most remain at the laboratory or proof-of-concept stage. Further studies on scalability, compatibility, and long-term stability will be essential to assess their commercial relevance and guide the transition toward practical applications.

If successfully translated into practical systems, interfacial regulation holds great promise to enable unprecedented levels of fast charging, long cycling life, and real-world viability for large-scale energy storage using AZIBs. A conceptual roadmap outlining promising interfacial design trends over the next 5–10 years is presented in Fig. 7 to guide future research priorities. Furthermore, the insights and strategies reviewed herein are expected to provide valuable guidance for advancing not only other multivalent-ion battery systems (where ion size, solvation structures, and interfacial phenomena similarly dictate performance) but also conversion-type chemistries such as Zn–S and $Zn–I_2$ batteries, in which interfacial storage processes play an increasingly dominant role.

Conflicts of interest

There are no conflicts to declare.

Data availability

No primary research results, software or code have been included and no new data were generated or analysed as part of this review.

Acknowledgements

References

1 X. Jia, C. Liu, Z. G. Neale, J. Yang and G. Cao, *Chem. Rev.*, 2020, **120**, 7795–7866.
2 C. Xu, B. Li, H. Du and F. Kang, *Angew. Chem., Int. Ed.*, 2012, **51**, 933–935.
3 D. Kundu, B. D. Adams, V. Duffort, S. H. Vajargah and L. F. Nazar, *Nat. Energy*, 2016, **1**, 16119.

4   H. Pan, Y. Shao, P. Yan, Y. Cheng, K. S. Han, Z. Nie, C. Wang, J. Yang, X. Li, P. Bhattacharya, K. T. Mueller and J. Liu, *Nat. Energy*, 2016, **1**, 16039.

5   W. Zong, J. Li, C. Zhang, Y. Dai, Y. Ouyang, L. Zhang, J. Li, W. Zhang, R. Chen, H. Dong, X. Gao, J. Zhu, I. P. Parkin, P. R. Shearing, F. Lai, K. Amine, T. Liu and G. He, *J. Am. Chem. Soc.*, 2024, **146**, 21377–21388.

6   R. Chen, W. Zhang, C. Guan, Y. Zhou, I. Gilmore, H. Tang, Z. Zhang, H. Dong, Y. Dai, Z. Du, X. Gao, W. Zong, Y. Xu, P. Jiang, J. Liu, F. Zhao, J. Li, X. Wang and G. He, *Angew. Chem., Int. Ed.*, 2024, **63**, e202401987.

7   S. Mariyappan, T. Marchandier, F. Rabuel, A. Iadecola, G. Rousse, A. V. Morozov, A. M. Abakumov and J. M. Tarascon, *Chem. Mater.*, 2020, **32**, 1657–1666.

8   X. Zhang, S. Yang, X. Shan, S. Li and S. Tang, *Phys. Chem. Chem. Phys.*, 2019, **21**, 23697–23704.

9   H. Yao, H. Yu, Y. Zheng, N. W. Li, S. Li, D. Luan, X. W. D. Lou and L. Yu, *Angew. Chem., Int. Ed.*, 2023, **62**, e202315257.

10 F. Wan, Y. Zhang, L. Zhang, D. Liu, C. Wang, L. Song, Z. Niu and J. Chen, *Angew. Chem., Int. Ed.*, 2019, **58**, 7062–7067.

11 L. Wang, S. Yan, C. D. Quilty, J. Kuang, M. R. Dunkin, S. N. Ehrlich, L. Ma, K. J. Takeuchi, E. S. Takeuchi and A. C. Marschilok, *Adv. Mater. Interfaces*, 2021, **8**, 2002080.

12 R. W. Chen, C. Y. Zhang, J. W. Li, Z. J. Du, F. Guo, W. Zhang, Y. H. Dai, W. Zong, X. Gao, J. X. Zhu, Y. Zhao, X. H. Wang and G. J. He, *Energy Environ. Sci.*, 2023, **16**, 2540–2549.

13 X. M. Li, X. Y. Wang, L. T. Ma and W. Huang, *Adv. Energy Mater.*, 2022, **12**, 2202068.

14 S. Chen, D. Ji, Q. Chen, J. Ma, S. Hou and J. Zhang, *Nat. Commun.*, 2023, **14**, 3526.

15 L. Cao, D. Li, T. Pollard, T. Deng, B. Zhang, C. Yang, L. Chen, J. Vatamanu, E. Hu, M. J. Hourwitz, L. Ma, M. Ding, Q. Li, S. Hou, K. Gaskell, J. T. Fourkas, X. Q. Yang, K. Xu, O. Borodin and C. Wang, *Nat. Nanotechnol.*, 2021, **16**, 902–910.

16 C. Liu, Q. Li, Y. Lin, Z. Wei, Y. Yang, C. Han, M. Zhu, H. Zhang and H. Li, *Nano Res. Energy*, 2023, **2**, e9120064.

17 Q. Zhang, J. Luan, X. Huang, Q. Wang, D. Sun, Y. Tang, X. Ji and H. Wang, *Nat. Commun.*, 2020, **11**, 3961.

18 Y. X. Zhang, Y. Z. Y. Chen, Y. Jiang, J. Wang, X. Y. Zheng, B. Han, K. S. Xia, Q. Gao, Z. Cai, C. G. Zhou and R. M. Sun, *Adv. Funct. Mater.*, 2023, **33**, 2212785.

19 D. Li, L. Cao, T. Deng, S. Liu and C. Wang, *Angew. Chem., Int. Ed.*, 2021, **60**, 13035–13041.

20 W. Zhang, Y. Dai, R. Chen, Z. Xu, J. Li, W. Zong, H. Li, Z. Li, Z. Zhang, J. Zhu, F. Guo, X. Gao, Z. Du, J. Chen, T. Wang, G. He and I. P. Parkin, *Angew. Chem., Int. Ed.*, 2023, **62**, e202212695.

21 W. Du, E. H. Ang, Y. Yang, Y. Zhang, M. Ye and C. C. Li, *Energy Environ. Sci.*, 2020, **13**, 3330–3360.

22 J. Shin, J. Lee, Y. Park and J. W. Choi, *Chem. Sci.*, 2020, **11**, 2028–2044.

23 W. Zhang and G. He, *Angew. Chem., Int. Ed.*, 2023, **62**, e202218466.

24 X. Zhang, L. Zhang, X. Jia, W. Song and Y. Liu, *Nano-Micro Lett.*, 2024, **16**, 75.

25 T. Wang, S. Tang, Y. Xiao, W. Xiang and J. S. Yu, *Energy Environ. Sci.*, 2025, **18**, 545–578.

26 X. Wang, B. Liu, Z. Xu, Y. Zhou, Y. Yang, H. Pan and G. Wang, *Adv. Energy Mater.*, 2025, **15**, 2405253.

27 P. H. Liang, T. F. Xu, K. J. Zhu, Y. Rao, H. J. Zheng, M. Wu, J. T. Chen, J. S. Liu, K. Yan, J. Wang and R. F. Zhang, *Energy Storage Mater.*, 2022, **50**, 63–74.

28 P. Cai, K. L. Wang, X. He, Q. X. Li, Z. C. Zhang, M. J. Li, H. M. Li, M. Zhou, W. Wang and K. Jiang, *Energy Storage Mater.*, 2023, **60**, 102835.

29 Y. Wang, J. Song and W. Y. Wong, *Angew. Chem., Int. Ed.*, 2023, **62**, e202218343.

30 X. L. Guo, C. G. Li, X. Y. Wang, Z. H. Li, H. Zeng, P. Hou, M. G. Xie, Y. X. Li, Z. Shi and S. H. Feng, *Sci. China: Chem.*, 2023, **66**, 1406–1416.

31 H. A. Zhai, H. B. Liu, Y. F. Zhang, J. J. Wen, W. Y. Yang, H. T. Xu, X. T. Yan, W. C. Peng and J. P. Liu, *J. Mater. Sci. Technol.*, 2024, **188**, 183–190.

32 X. Liu, W. Ni, Y. Wang, Y. Liang, B. Wu, G. Xu, X. Wei and L. Yang, *Small*, 2022, **18**, e2105796.

33 B. Q. Xiao, J. Chen, C. F. Hu, L. S. Mou, W. J. Yang, W. H. He, Z. B. Lu, S. L. Peng and J. J. Huang, *Adv. Funct. Mater.*, 2023, **33**, 2211679.

34 G. Q. Yuan, X. Wei, Y. C. Su, T. Y. Zhou, J. L. Hu, Y. An, S. L. Zhou, W. Q. Zhao, J. Xia and Y. Y. Liu, *Small*, 2024, **20**, e2308851.

35 N. U. R. Lashari, A. Kumar, I. Ahmed, J. Zhao, A. Hussain, U. Ghani, G. Luo, G. Yasin, M. A. Mushtaq, D. Liu and X. Cai, *Small*, 2024, **20**, e2309029.

36 N. Jiang, Y. Zeng, Q. Yang, P. D. Lu, K. Q. Qu, L. H. Ye, X. J. Lu, Z. Q. Liu, X. X. Li, Y. C. Tang, J. C. Cao, S. M. Chen, C. Y. Zhi and J. S. Qiu, *Energy Environ. Sci.*, 2024, **17**, 8904–8914.

37 C.-C. Chen and J. Maier, *Nat. Energy*, 2018, **3**, 102–108.

38 Y. Dai, X. Liao, R. Yu, J. Li, J. Li, S. Tan, P. He, Q. An, Q. Wei, L. Chen, X. Hong, K. Zhao, Y. Ren, J. Wu, Y. Zhao and L. Mai, *Adv. Mater.*, 2021, **33**, e2100359.

39 D. X. Liu, W. J. Wang, S. M. Li, X. J. Shen, H. J. Xie and H. Xu, *Adv. Funct. Mater.*, 2024, **34**, 2402584.

40 W. Zhong, Z. Y. Shen, J. L. Mao, S. C. Zhang, H. Cheng, Y. Kim and Y. Y. Lu, *Energy Environ. Sci.*, 2024, **17**, 2059–2068.

41 Q. Gou, H. Luo, Y. Zheng, Q. Zhang, C. Li, J. Wang, O. Odunmbaku, J. Zheng, J. Xue, K. Sun and M. Li, *Small*, 2022, **18**, e2201732.

42 L. Y. Ding, L. Wang, J. C. Gao, T. R. Yan, H. T. Li, J. Mao, F. Song, S. Fedotov, L. Y. Chang, N. Li, Y. F. Su, T. F. Liu and L. Zhang, *Adv. Funct. Mater.*, 2023, **33**, 2301648.

43 M. L. Chen, M. Zhou, Q. Y. Wang, C. Xu, S. Wang, J. Ning, T. Q. Wang, K. L. Wang and K. Jiang, *Adv. Funct. Mater.*, 2025, **35**, 2414032.

44 Y. Dai, C. Zhang, J. Li, X. Gao, P. Hu, C. Ye, H. He, J. Zhu, W. Zhang, R. Chen, W. Zong, F. Guo, I. P. Parkin, D. J. L. Brett, P. R. Shearing, L. Mai and G. He, *Adv. Mater.*, 2024, **36**, e2310645.

45 Q. Sun, H. Cheng, C. Sun, Y. Liu, W. Nie, K. Zhao, X. Lu and J. Zhou, *ACS Appl. Mater. Interfaces*, 2021, **13**, 60035–60045.

This journal is © The Royal Society of Chemistry 2025

Energy Environ. Sci., 2025, **18**, 9018–9030 | **9029**

46 X. Zheng, Y. Zheng, Y. Tao, X. Zheng, Z. Chen, X. Wang, M. Shang, J. Du, S. Wu, Y. Pang, F. Wang and Z. Shen, *J. Alloys Compd.*, 2025, **1010**, 178140.

47 X. D. Jiang, T. D. Wang, M. Z. Ji, D. Ji, S. Y. Deng, G. H. Gao, J. Shen and G. M. Wu, *Adv. Funct. Mater.*, 2025, **35**, 2420686.

48 J. Zhang, L. Pan, L. Jia, J. Dong, C. You, C. Han, N. Tian, X. Cheng, B. Tang, Q. Guan, Y. Zhang, B. Deng, L. Lei, M. Liu, H. Lin and J. Wang, *Nano Lett.*, 2025, **25**, 3756–3765.

49 A. H. Wu, S. J. Zhang, Q. H. Li, W. X. Xue, C. Y. Li, B. J. Xi, W. T. Mao, K. Y. Bao and S. L. Xiong, *Adv. Energy Mater.*, 2025, **15**, 2404450.

50 G. J. Yang, Q. Zhang, Z. L. Liu, J. Song, Z. Y. Yin, Y. X. Zhao, S. H. Jiang, J. Q. Han, X. Li, H. Q. Yang, S. J. He and Z. X. Pei, *Adv. Energy Mater.*, 2025, 2501358.

51 J. Dong, X. Cheng, H. Yang, H. Li, H. Liu, L. Jia, Y. Zhang, Q. Guan, J. Jia, F. Wu, J. Zhang, M. Liu, H. Lin and J. Wang, *Adv. Mater.*, 2025, **37**, e2501079.

52 X. Guo, Q. Peng, R. Yang, G. Cao, J. Wen, K. Shin, Y. Zheng, S. Tunmee, C. Zou, Y. Zheng, X. Zhou and Y. Tang, *Natl. Sci. Rev.*, 2025, **12**, nwaf070.

53 J. Yan, H. Dou, M. Su, M. Xu, S. Liu, S. Qin, B. Zhang, K. Zong, L. Tan, X. Wang and Z. Chen, *Angew. Chem., Int. Ed.*, 2025, **64**, e202505372.

54 X. Shi, J. Xie, J. Wang, S. Xie, Z. Yang and X. Lu, *Nat. Commun.*, 2024, **15**, 302.

55 X. Yu, M. Chen, Z. Li, X. Tan, H. Zhang, J. Wang, Y. Tang, J. Xu, W. Yin, Y. Yang, D. Chao, F. Wang, Y. Zou, G. Feng, Y. Qiao, H. Zhou and S. G. Sun, *J. Am. Chem. Soc.*, 2024, **146**, 17103–17113.

56 J. Lu, T. Wang, J. Yang, X. Shen, H. Pang, B. Sun, G. Wang and C. Wang, *Angew. Chem., Int. Ed.*, 2024, **63**, e202409838.

57 D. W. Smith, *J. Chem. Educ.*, 1977, **54**, 540–542.

58 Z. X. Zhou, M. M. Han, Y. D. Sun, Y. X. Cui, S. A. El-khodary, D. H. L. Ng, J. B. Lian and J. M. Ma, *Adv. Funct. Mater.*, 2024, **34**, 2308834.

59 L. Wang, K. W. Huang, J. Chen and J. Zheng, *Sci. Adv.*, 2019, **5**, eaax4279.

60 Z. L. Li, S. Ganapathy, Y. L. Xu, Z. Zhou, M. Sarilar and M. Wagemaker, *Adv. Energy Mater.*, 2019, **9**, 1900237.

61 S. Li, C. Huang, L. Gao, Q. Shen, P. Li, X. Qu, L. Jiao and Y. Liu, *Angew. Chem., Int. Ed.*, 2022, **61**, e202211478.

62 Y. F. Yuan, R. Sharpe, K. He, C. H. Li, M. T. Saray, T. C. Liu, W. T. Yao, M. Cheng, H. L. Jin, S. Wang, K. Amine, R. Shahbazian-Yassar, M. S. Islam and J. Lu, *Nat. Sustain.*, 2022, **5**, 890–898.

63 H. Chen, C. Dai, F. Xiao, Q. Yang, S. Cai, M. Xu, H. J. Fan and S. J. Bao, *Adv. Mater.*, 2022, **34**, e2109092.

64 H. L. Pan, Y. Y. Shao, P. F. Yan, Y. W. Cheng, K. S. Han, Z. M. Nie, C. M. Wang, J. H. Yang, X. L. Li, P. Bhattacharya, K. T. Mueller and J. Liu, *Nat. Energy*, 2016, **1**, 16039.

65 L. Wang, J. Yan, Y. Hong, Z. Yu, J. Chen and J. Zheng, *Sci. Adv.*, 2023, **9**, eadf4589.

66 M. L. Chen, X. He, M. Zhou, J. Ning, Z. D. Zhang, S. L. Cao, T. Q. Wang, K. L. Wang and K. Jiang, *Adv. Energy Mater.*, 2024, **14**, 2400724.

67 C. Lee, Y. Hong, D. Kim, Y. Lim, J. W. Choi and S. Y. Chung, *Adv. Funct. Mater.*, 2023, **33**, 2303763.

68 Q. Chen, X. Lou, Y. Yuan, K. You, C. Li, C. Jiang, Y. Zeng, S. Zhou, J. Zhang, G. Hou, J. Lu and Y. Tang, *Adv. Mater.*, 2023, **35**, e2306294.

69 F. Wang, L. E. Blanc, Q. Li, A. Faraone, X. Ji, H. H. Chen-Mayer, R. L. Paul, J. A. Dura, E. Y. Hu, K. Xu, L. F. Nazar and C. S. Wang, *Adv. Energy Mater.*, 2021, **11**, 2102016.

70 S. Deng, H. Li, B. Chen, Z. Xu, Y. Jiang, C. Li, W. Xiao and X. Yan, *Chem. Eng. J.*, 2023, **452**, 139115.

71 S. Hou, J. Luo, W. Gong, Y. Xie, X. Zhou, F. Yue, J. Shen, C. Li, L. Wei, F. Xu and Q. Zhang, *ACS Nano*, 2024, **18**, 31524–31536.

72 S. Jin, F. Duan, X. Wu, J. Li, X. Dan, X. Yin, K. Zhao, Y. Wei, Y. Sui, F. Du and Y. Wang, *Small*, 2022, **18**, e2205462.

73 Q. He, T. Hu, Q. Wu, C. Wang, X. Han, Z. Chen, Y. Zhu, J. Chen, Y. Zhang, L. Shi, X. Wang, Y. Ma and J. Zhao, *Adv. Mater.*, 2024, **36**, e2400888.

74 G. Mahendra, R. Roy and A. K. Singh, *J. Power Sources*, 2024, **624**, 235515.

75 D. Guo, J. Sun, C. Wang, H. Quan, H. Lu, Y. Wei, C. Sun and S. Wang, *Angew. Chem., Int. Ed.*, 2025, **64**, e202505102.

76 J. Li, K. Ge, A. O. Grammenos, P. L. Taberna, P. Simon, M. Antonietti and M. Odziomek, *Adv. Mater.*, 2025, **37**, e2502422.

77 Y. H. Dai, R. H. Lu, C. Y. Zhang, J. T. Li, Y. F. Yuan, Y. Mao, C. M. Ye, Z. J. Cai, J. X. Zhu, J. H. Li, R. H. Yu, L. M. Cui, S. Y. Zhao, Q. Y. An, G. J. He, G. I. N. Waterhouse, P. R. Shearing, Y. Ren, J. Lu, K. Amine, Z. Y. Wang and L. Q. Mai, *Nat. Catal.*, 2024, **7**, 776–784.

78 J. Wang, X. Gao, Y. Wang, R. Pan, Z. Liu, X. Liu, H. Xie, F. Yu, G. Wang and T. Gu, *Nano Res. Energy*, 2024, **3**, e9120124.

9030 | *Energy Environ. Sci.*, 2025, **18**, 9018–9030

This journal is © The Royal Society of Chemistry 2025